

PAPER • OPEN ACCESS

Simulation of capillary-driven kinetics with multi-phase-field and lattice Boltzmann method

To cite this article: Raphael Schiedung *et al* 2020 *Modelling Simul. Mater. Sci. Eng.* **28** 065008

View the [article online](#) for updates and enhancements.

239th ECS Meeting

with the 18th International Meeting on Chemical Sensors (IMCS)

ABSTRACT DEADLINE: DECEMBER 4, 2020



May 30-June 3, 2021

SUBMIT NOW →

Simulation of capillary-driven kinetics with multi-phase-field and lattice Boltzmann method

Raphael Schiedung¹ , Marvin Tegeler¹,
Dmitry Medvedev^{2,3} and Fathollah Varnik¹

¹ Ruhr Universität Bochum, Interdisciplinary Center for Advanced Materials Simulation (ICAMS), Universitätsstr. 150, 44801 Bochum, Germany

² Lavrentyev Institute of Hydrodynamics SB RAS, Lavrentyev prosp. 15, 630090, Novosibirsk, Russia

³ Novosibirsk State University, Pirogova str. 2, 630090, Novosibirsk, Russia

E-mail: raphael.schiedung@rub.de and fathollah.varnik@rub.de

Received 19 February 2020, revised 28 April 2020

Accepted for publication 11 June 2020

Published 15 July 2020



CrossMark

Abstract

We propose a combined computational approach based on the multi-phase-field and the lattice Boltzmann method for the motion of solid particles under the action of capillary forces. The accuracy of the method is analyzed by comparison with the analytic solutions for the motion of two parallel plates of finite extension connected by a capillary bridge. The method is then used to investigate the dynamics of multiple spherical solid bodies connected via capillary bridges. The amount of liquid connecting the spheres is varied, and the influence of the resulting liquid-morphology on their dynamics is investigated. It is shown that the method is suitable for a study of liquid-phase sintering which includes both phase transformation and capillary driven rigid body motion.

Keywords: liquid-phase sintering, phase-field, lattice Boltzmann, multi-phase fluids, wetting, capillarity

(Some figures may appear in colour only in the online journal)

1. Introduction

During the sintering process, liquids can form intricate structures and bridges between multiple solid particles which by themselves can have a complex topology and can form large



Original content from this work may be used under the terms of the [Creative Commons Attribution 4.0 licence](https://creativecommons.org/licenses/by/4.0/). Any further distribution of this work must maintain attribution to the author(s) and the title of the work, journal citation and DOI.

structures with other solid particles. These capillary bridges between the solid particles lead to compaction of the sample. Various theoretical approaches consider the force exerted by capillary bridges on solids. An early analysis of capillary forces in liquid-phase sintering processes of spherical particles can be found in [1]. The elementary capillary bridge between two identical spheres offers already a wide range of possible investigations such as its shape, the capillary force exerted by the bridge on a spherical particle, or the wetting angle and the amounts of liquid for which the bridge exists before its point of rupture [2–4]. A more complex scenario is considered in recent works [5, 6] where also the effect of unequal sized spheres is investigated.

Villanueva *et al* [7] proposed a combined approach of a multicomponent and multi-phase-field model with the Navier–Stokes equations for the simulation of liquid-phase sintering. Also within the lattice Boltzmann methods [8, 9], models have been proposed to simulate the dynamics of solid particles, multiple fluids [10, 11], and more recently with the integration of liquid–gas interfaces with solid bodies [12].

The so-called Shan–Chen model [13, 14] for multiphase and multicomponent flows has been further developed and used by a large community to study various types of problems such as flow of immiscible fluids through a porous medium [15, 16], interaction of particles with fluid–fluid interfaces [17] and the response of ellipsoidal particles adsorbed at fluid–fluid interfaces to external magnetic fields [18], to name just a few examples.

Recently, Sun and Sakai have performed an intensive numerical study on capillary bridges between two, three, and four spherical particles, where they used the so-called direct numerical simulation method [19]. In the special case of two spherical bodies, they also studied the motion of the solid spheres under the action of capillary forces.

However, we are not aware of any work addressing the full multiphysics problem of liquid phase sintering (LPS). To see the rich variety of physical phenomena involved in LPS, consider a powder mixture of two metallic materials which is pressed into a green body. As the material is gradually heated, diffusion is enhanced and particles at contact undergo solid-phase sintering process. This leads to the formation of solid bridges between particles, which connect them together. The strength of this initial sintering depends on the material and the heating rate. As temperature increases further, one of the two powder components (the so-called soft metal) starts to melt and forms liquid capillary bridges between the remaining (hard) solid particles. Due to the random distribution of distances and the formed liquid bridges, solid particles undergo a kind of random motion and rearrange, thereby leading to a densification of the sample. This process of particle rearrangement depends both on capillary forces exerted by the liquid bridges, particle mass, and on the possible existence of solid bridges formed during the initial solid-phase sintering. These solid bonds hinder the rearrangement dynamics and are usually undesired in liquid phase sintering. In this regard, the dissolution of solid bridges in the soft-metal liquid offers an interesting physical mechanism in favor of a faster dynamics. All these processes have to be considered when simulating liquid-phase sintering.

The present model aims at addressing all these multiphysics aspects. We present a hybrid approach based on a combination of the multi-phase-field method and the lattice Boltzmann method (section 3). The phase-field method is used to treat physical processes involving solid phases, while the lattice Boltzmann part is responsible for liquid–vapor coexistence and the dynamics of fluid. To keep the focus of the present manuscript as sharp as possible, we let aside solid-phase sintering, which has already been addressed in a separate study [20]. Further, investigation of the dissolution process is postponed to future work. All other aspects are the subject of the present manuscript.

We show the reliability of the model, by comparing the obtained results with analytic solutions for the force and motion of two finite parallel plates connected by a cylindrical liquid bridge. The analytic solutions are introduced in section 2. In addition to the comparison with the analytic solution, we show an investigation of the resolution dependence of the capillary force acting on the two plates, their motion due to the action of the capillary force and the wetting angle (see section 4.2). Beyond these benchmark scenarios, we study the dynamics of two, three, and four spherical bodies under the action of the capillary force for various amounts of liquid fractions in section 4.3. By doing this investigation, we show the differences in dynamics but also the similarities. We summarize the results in the section 5.

2. Capillary forces on solids

As a test for our model, we consider the force of a single capillary bridge on two parallel plates and the resulting motion of these plates in section 2.1. An introductory example is the topology of a capillary bridge between two spherical bodies which depends on the amount of liquid and the wetting angle. We discuss this dependency in section 2.2.

2.1. Capillary bridge between two plates

In principle, a capillary bridge between two plates can form a variety of different surface shapes with a constant curvature which depends on the wetting angle, the distance between the plates, and the amount of liquid between the plates. These shapes can be separated into two basic classes, convex and concave bridges. In addition to this classification, analytic descriptions of these shapes can be found, such as a sphere, a cylinder, or a catenoid [21].

Here, we consider only simple examples to test our model, a planar capillary bridge with a 90° wetting angle, and a cylindrical bridge with the same wetting angle. For simplicity, the planar capillary bridge can be considered as a 2D problem. Nevertheless, the planar capillary bridge example is simulated in a three-dimensional setup with periodic boundaries.

This approach not only offers the possibility to calculate the resulting force on the plates (see section 2.1.1) but also allows the integration of the equation of motion to obtain an approximate solution for the dynamics at early times as the plates start to move toward each other (see section 2.1.2).

2.1.1. Force on the plates. We consider two scenarios as illustrated in figure 1. The depicted capillary bridges are determined by their radius R , the distance between the plates h and the wetting angle Θ . To calculate the resulting force on the plates, we use the total differential of the internal energy U of such a capillary bridge which is given by

$$dU = \sigma_{SL} dA_{SL} + \sigma_{SV} dA_{SV} + \sigma_{LV} dA_{LV} - p_V dV_V - p_L dV_L. \quad (1)$$

σ_{SL} denotes the surface tension of the solid–liquid interface, σ_{SV} of the solid–vapor interface, and σ_{LV} of the liquid–vapor interface with the associated areas A_{SL} , A_{SV} , and A_{LV} . p_V and p_L are pressures of the vapor and liquid phases with the respective volumes V_V and V_L . Because of the considered geometry, one can see that $dA_{SV} = -dA_{SL}$ and $dV_V = -dV_L$ so that equation (1) can be simplified

$$dU = -(\sigma_{SV} - \sigma_{SL}) dA_{SL} + \sigma_{LV} dA_{LV} - \Delta p dV_L, \quad (2)$$

where $\Delta p = p_L - p_V$ is the pressure difference between vapor and liquid.

The equilibrium shape of the liquid minimizes the internal energy U . In the absence of solids, in the case of a spherical liquid droplet ($dA_{SL} = 0$), it can be shown by minimization

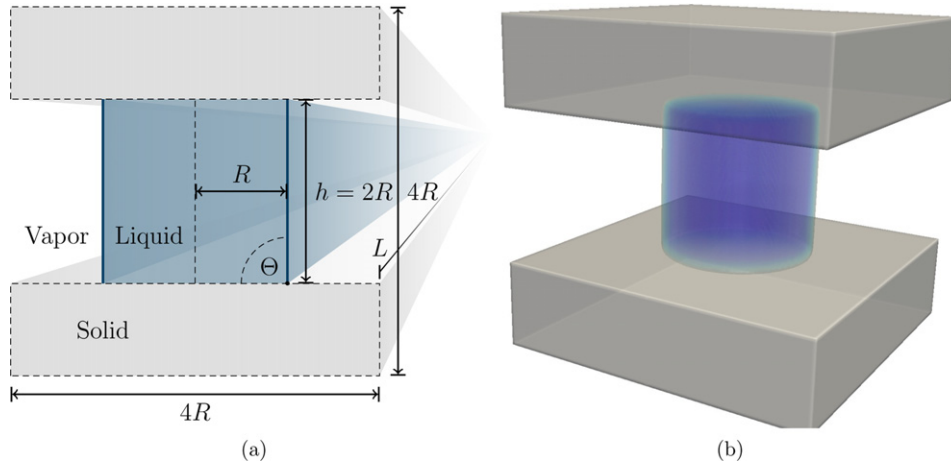


Figure 1. (a) A schematic representation of a planar capillary bridge between two plates with the thickness R , initial radius of the liquid bridge R , and wetting angle $\Theta = \pi/2$. (b) The initial simulation setup of a cylindrical capillary bridge. Depicted are the surfaces of the solid plates in gray and the liquid surface in blue.

of the total internal energy, i.e., by setting $dU = 0$, that the pressure difference between vapor and liquid is proportional to the curvature κ of the surface,

$$\Delta p = \sigma_{LV}\kappa, \quad (3)$$

which is called the Young–Laplace equation. We consider here the curvature as the sum of the principal curvatures $\kappa = \sum_i^{D-1} \kappa_i$ where D denotes the dimension. Because a pressure gradient would result in a motion of the fluid, equation (3) states that the equilibrium surface of the liquid must be of constant curvature. In the presence of solid–fluid interfaces, the energy minimization principle delivers also, the well-known Young’s equation $\cos \Theta = (\sigma_{SV} - \sigma_{SL})/\sigma_{LV}$, where Θ is the wetting angle.

We consider a wetting of 90° so that the first term in equation (2) vanishes. Further, we neglect the effect of evaporation due to a change of liquid–vapor interface curvature so that the liquid volume can be considered as constant and hence the last term in equation (2) vanishes also. The change of the internal thus determined by the change of liquid–vapor interface area

$$dU = \sigma_{LV} dA_{LV}. \quad (4)$$

In the planar case (figure 1(a)), the magnitude of the force is then given by

$$F_p = 2\sigma_{LV}L, \quad (5)$$

where L is the length of the planar capillary wall. Later, in the simulation, we use periodic boundary conditions. L would then be the length of the simulation domain perpendicular to the depicted planar capillary bridge in figure 1(a).

For the cylindrical capillary bridge (see figure 1(b)), one obtains

$$F_c = \pi\sigma_{LV}R. \quad (6)$$

In the following, we drop the index of σ_{LV} to simplify the notation. A more detailed derivation can be found in appendix A.

2.1.2. Motion of the plates. Based on the analytic descriptions of the forces equations (6) and (5), the distance h of the plates as a function of time can be calculated. This dynamic solution provides a more sophisticated benchmark for the dynamics of the present method. To reduce the complexity of the analysis, we assume that the motion of the plates is slow compared to the motion of the fluid. In this case, the bridge can be assumed to remain in its cylindrical shape during the motion of the plates. Also, the kinetic energy of the liquid can be neglected. These assumptions are valid if the mass of the plates is much larger than the mass of the liquid.

In the planar case, the computation is simple because the integral of the constant force equation (5) delivers

$$h_p = h_0 - \frac{1}{2} \frac{F_p}{m} t^2 - \frac{1}{2} \frac{F_p}{m} t^2 \quad (7a)$$

$$h_p = h_0 - \frac{2\sigma L}{m} t^2, \quad (7b)$$

where m is the mass of a single plate, h_0 the initial distance, and t the time. The factor of two accounts for the fact that both plates are mobile and subject to the same magnitude of the force.

In the cylindrical case, the function $h_c(t)$ can be approximated with

$$h_c(t) \approx h_0 - \frac{\pi\sigma R_0}{m} t^2 \quad (8)$$

where the change of the capillary radius has been neglected.

2.2. Liquid bridge between two spherical solids

As an introductory scenario, we consider a liquid bridge between two spherical solids of the same size in contact with each other. Even in this simplified case, the analytic description of the bridge can be complicated. The possible equilibrium configurations of such a system are determined by the wetting angle and the liquid volume fraction $c = V_L / (V_L + V_S)$, where V_S is the solid volume. The choice of these two parameters offers the possibility to discuss the topology of this system independent of its scale. For two spherical solids in contact, two ideal solutions for the topology of the liquid bridge exist, a spherical bridge in the limit of a large liquid volume fraction ($c = 0.75, \Theta = 0$) and a cylindrical bridge for the other extreme case of low liquid content ($c = 0.2, \Theta = 0$).

Strictly speaking, both these types of bridges are symmetric with regard to rotation around the axis joining the centers of the two particles. For hydrophilic solids considered in this work, small amounts of liquid and small contact angles lead to liquid bridges with a negative curvature. An example of this case is shown in the left bottom corner of figure 2. In the other limit of large liquid volumes, the liquid–vapor interface has a positive curvature and the capillary bridge looks like a portion of a sphere lacking the volume occupied by the solids (see the top right image in figures 2 and B1). A liquid bridge shaped like a cylinder, which lacks a portion occupied by the two solids (see figure B3), marks the point between both limits where one of the two principal curvatures changes its sign. To approximate a bridge as being either cylindrical or spherical shaped, the parameter ranges for the existence of both shapes provide valuable criteria (depicted as lines in figure 2). A detailed account of these cases is given in appendix B. In the following, we provided an overview of the findings.

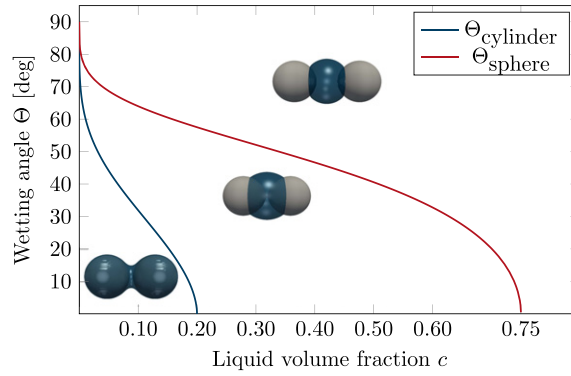


Figure 2. The wetting angle for the limiting cases of spherical and cylindrical liquid bridges as a function of the liquid volume fraction (see equations (9) and (10)). The area between these two solutions corresponds to more complex (mixed) bridge shapes. These two functions thereby classify the topology of the bridges into three types as illustrated by pictures obtained from simulation. Note that, in these simulations, particles are allowed to move under the action of capillary forces.

By calculating the wetting angle between a spherical liquid bridge as a function of the liquid volume fraction, one obtains the relation

$$\Theta_s = \arccos\left(\frac{\chi_s^2 - 2}{2}\right) - \arccos\left(\frac{\chi_s}{2}\right) \quad (9a)$$

$$\chi_s = \frac{2}{\sqrt[4]{3}} \frac{\sqrt{(1-c)}\sqrt{c(1-c)}}{1-c}. \quad (9b)$$

The same way, a relationship between the wetting angle and the liquid volume fraction can be found in the case of a cylindrical bridge,

$$\Theta_c = \frac{\pi}{2} - \arccos(1 - \chi_c) \quad (10a)$$

$$\chi_c = -\cos\left(\frac{1}{3} \arccos\left(\frac{1-9c}{1-c}\right) + \frac{\pi}{3}\right) + \frac{1}{2}. \quad (10b)$$

A derivation of equations (9) and (10) can be found in appendix B. Equations (9) and (10) are depicted in figure 2.

However, more interesting are the parameter regions delimited by the spherical and cylindrical solutions. For all pairs of wetting angles and liquid volume fraction below the cylindrical solution in figure 2, one of the radii of curvature of the bridge becomes negative. Between the cylindrical and the spherical solution lies the region of parameters where the bridges have a convex shape but not yet a spherical one.

In the region above the spherical solution, the spherical solids are not brought into contact by the liquid capillary bridge. Instead, the solids are separated by the bridge. As long as the solid surface is not entirely hydrophobic, the spherical solids will not separate from the liquid bridge. Furthermore, the liquid bridge has a spherical shape for liquid volume fractions and wetting-angles above the plotted spherical solution.

To illustrate these possible shapes, pictures obtained from simulation are added to figure 2 according to their contact angle and liquid volume fraction. The pictures are obtained from

simulations with the method described in section 3. Note that the particles are not kept in a fixed position but are allowed to move under the action of capillary forces along their connecting axis line until the equilibrium configuration is reached. As a result, the liquid fraction and the wetting angle influence both the shape of the liquid bridge and the distance between the spherical solids.

In the following, we focus on the investigation of the parameter range below the spherical solution.

3. Numerical model

In the following section, we give a brief compendium of the implemented model which consists basically of a combined approach of the multi-phase-field method for the modeling of solid phases, including solid-solid as well as solid-liquid phase transformation, and the lattice Boltzmann method for modeling the fluid flow, liquid-vapor phase separation, and solid-fluid interaction. An overview of the modeling of solids and their dynamics is shown in section 3.1. The lattice Boltzmann method is discussed in section 3.2 with its coupling to the dynamics of solid bodies. In section 3.3, we explore some numerical aspects and parameters.

3.1. Modeling of solids

The phase-field method is a method for solving interfacial problems, and it has been applied to various kinds of problems such as solidification [22], grain-growth [23], surface or phase-boundary diffusion [20], and elastic deformation of solid bodies due to surface tension [24]. Here, we use the well-established multi-phase-field method which is summed up in two review articles [25, 26].

The model allows us to distinguish and track each solid particle while for example being deformed or being in the process of a phase transition. This tracking of a rigid body and its topology is achieved by a continuous indicator function called the phase-field ϕ_α . Given a point \vec{x} in space, $\phi_\alpha(\vec{x}) = 1$ means that the phase α is present at that point and $\phi_\alpha(\vec{x}) = 0$ means that it is not. All values of ϕ_α between 0 and 1 are considered as surface or interface of the particle or phase α with its surroundings. The considered system may consist of N phases so that all phase-fields must satisfy the sum constraint $\sum_\alpha \phi_\alpha = 1$. A rigid body B must consist of at least one phase-field, but it may even consist of multiple phase-fields. We consider the dynamics of the solid particles as modeled by the advection of the phase-fields according to the velocity of the solid bodies. The velocity is calculated according to forces and torques acting on the bodies (see section 3.1.1). Between two colliding bodies, a repulsive force is used (see section 3.1.2).

As mentioned above, the phase-field method is commonly used to describe phenomena such as phase transformations or even surface/phase-boundary diffusion which may lead to growth, shrinkage or deformation of solid particles. These processes can be considered with the present model, but they are not considered in this work, and the reader is referred to [20, 25, 26].

3.1.1. Solid dynamics. Consider a rigid body B which is subject to the force \vec{F}_B and the torque \vec{T}_B . The center of mass \vec{X}_B of the solid body is accelerated with

$$\ddot{\vec{X}}_B = M_B^{-1} \vec{F}_B, \quad (11)$$

where M_B is the mass of the solid body. The angular velocity $\vec{\omega}_B$ changes with

$$\dot{\vec{\omega}}_B = \underline{I}_B^{-1} \vec{T}_B, \quad (12)$$

where \underline{I}_B is the tensor of inertia. The resulting velocity \vec{u}_B of B at the point \vec{x} can be calculated with

$$\vec{u}_B(\vec{x}) = \dot{\vec{X}}_B + \vec{\omega}_B \times (\vec{x} - \vec{X}_B). \quad (13)$$

Each of the phase-fields ϕ_α associated with the rigid body B is advected with

$$\dot{\phi}_\alpha = \vec{u}_B \cdot \nabla \phi_\alpha. \quad (14)$$

For the advection equation (14) of the phase-fields, we use a high-order scheme with directional splitting and a monotonized central flux limiter [27].

3.1.2. Solid–solid interactions. Collisions are nearly inevitable when simulating rigid bodies inside a dynamic fluid flow. Thus, we utilize a repulsive solid–solid interaction to account for collisions. This repulsive force between two rigid bodies is derived from a potential energy density $e(\vec{x}_i, \vec{x}_j)$ between a point \vec{x}_i of the rigid body B_1 and a point \vec{x}_j of the rigid body B_2

$$e(\vec{x}_i, \vec{x}_j) = e_0 \begin{cases} \left| \frac{\|\vec{x}_i - \vec{x}_j\| - r_c}{r_c} \right|^n & \text{if } \|\vec{x}_i - \vec{x}_j\| < r_c \\ 0 & \text{else} \end{cases} \quad (15)$$

where r_c is a characteristic interaction distance and the energy density e_0 determines the interactions strength. Furthermore, a point \vec{x} is considered to be a part of the solid body B if one of its associated phase-fields is non zero. The force density \vec{f}_{ij} of a rigid body B_1 at \vec{x}_j acting on a rigid body B_2 at \vec{x}_i can obtain as

$$\vec{f}(\vec{x}_i, \vec{x}_j) = \frac{\partial e(\vec{x}_i, \vec{x}_j)}{\partial (\vec{x}_i - \vec{x}_j)} \quad (16a)$$

$$= e_0 \frac{n}{r_c} \frac{\vec{x}_i - \vec{x}_j}{\|\vec{x}_i - \vec{x}_j\|} \left| \frac{\|\vec{x}_i - \vec{x}_j\| - r_c}{r_c} \right|^{n-1}. \quad (16b)$$

By the summation over all pairs of \vec{x}_i and \vec{x}_j within the characteristic interaction length, the resulting total forces on the rigid bodies can be calculated. To keep the solid–solid interaction as short ranged as possible, we have chosen $r_c = 3\Delta x$ and $n = 4$ in our simulations where Δx is the lattice spacing.

3.2. Modeling of fluids

We use for the simulation of fluids the lattice Boltzmann method which is summed up in section 3.2.1. The interaction of the fluid with the solid bodies is shown in section 3.2.2. In section 3.2.3, we introduce the implemented method for the liquid-vapor phase separation.

3.2.1. The lattice Boltzmann method. Consider the distribution function $f(\vec{x}, \vec{v}, t)$ which is the probability to find a pseudo particle at the position \vec{x} with the physical velocity \vec{v} at the time t [28]. The continuous velocity space \vec{v} is discretized with a finite number of physical velocities \vec{c}_i of the pseudo particles. Although many schemes have been proposed for the discretization of the velocity space, we only consider here the so-called three-dimensional twenty-seven velocity model (D3Q27) with

$$\vec{c}_i = \begin{cases} (0, 0, 0) & i = 0 \\ (\pm c, 0, 0), (0, \pm c, 0), (0, 0, \pm c) & i = 1, \dots, 6 \\ (\pm c, \pm c, 0), (0, \pm c, \pm c), (\pm c, 0, \pm c) & i = 7, \dots, 18 \\ (\pm c, \pm c, \pm c) & i = 19, \dots, 26 \end{cases} \quad (17)$$

where $c = \Delta x / \Delta t$ is a shorthand and Δt is the time step. The fluid density ρ is calculated as the sum of the distribution function overall velocities $\rho = \sum_i f_i$ where the shorthand $f_i(\vec{x}, t) \equiv f(\vec{x}, \vec{c}_i, t)$ has been used. Likewise, the fluid velocity \vec{u} is calculated as average overall physical velocities \vec{c}_i weighted by the amount of pseudo particles f_i with $\vec{u} = 1/\rho \sum_i \vec{c}_i f_i$. This way, the lattice Boltzmann equations can be written as

$$f_i^*(\vec{x}, t) = f_i(\vec{x}, t) - \frac{1}{\tau} [f_i(\vec{x}, t) - f_i^{\text{eq}}(\rho(\vec{x}, t), \vec{u}(\vec{x}, t))] + \Delta t F_i \quad (18a)$$

$$f_i(\vec{x}, t + \Delta t) = f_i^*(\vec{x} - \vec{c}_i \Delta t, t) \quad (18b)$$

which describe the collision step equation (18a) and the streaming step equation (18b) of the pseudoparticles, f_i . The right-hand side of equation (18a) consists of two parts, the relaxation of the distribution function towards the local equilibrium distribution f_i^{eq} and the forcing term F_i . The local equilibrium distribution function can be calculated with

$$f_i^{\text{eq}}(\rho, \vec{u}) = \rho w_i \left[1 - \frac{\vec{u} \cdot \vec{u}}{2c_s^2} + \frac{\vec{c}_i \cdot \vec{u}}{c_s^2} + \frac{(\vec{c}_i \cdot \vec{u})^2}{2c_s^4} \right], \quad (19)$$

which is a second-order expansion of the local Maxwell–Boltzmann distribution with the weights

$$w_i = \begin{cases} 8/27 & i = 0 \\ 2/27 & i = 1, \dots, 6 \\ 1/54 & i = 7, \dots, 18 \\ 1/216 & i = 19, \dots, 26. \end{cases} \quad (20)$$

τ is the relaxation time and c_s the speed of sound in the lattice Boltzmann fluid with $c_s = c/\sqrt{3}$.

We use the forcing term as published in [29] with

$$F_i = \left(1 - \frac{1}{2\tau} \right) w_i \left[\frac{\vec{c}_i - \vec{v}}{c_s^2} + \frac{\vec{c}_i \cdot \vec{v}}{c_s^4} \vec{c}_i \right] \cdot \vec{f}, \quad (21)$$

where \vec{f} is the local body force density acting on the fluid and \vec{v} is the fluid velocity which can be calculated with

$$\rho \vec{v} = \sum_i \vec{c}_i f_i + \frac{\Delta t}{2} \vec{F}. \quad (22)$$

We apply body force densities originating from the solid–fluid interaction (section 3.2.2) and from non-ideal fluid contributions (section 3.2.3) which cause a phase separation between the liquid and vapor phase.

3.2.2. Solid–fluid interaction. A rigid body and a fluid exert force on each other due to their motion and inertia. In the following, we introduce so-called ‘bounce-back’ method [30] which has been implemented.

To use this solid–fluid interaction method, a point in the simulation domain has to be either solid or liquid. Because the phase-field method uses a continuous transition between two phases, a point is considered to be solid if the phase-field representing the fluid phase content is less than 0.05. For this choice of the cut-off value for ‘solidity’ and moderate velocities studied in this work, no staircase effect is not visible. Moreover, a certain, however small, amount of liquid always remains between two solid bodies so that direct solid-solid contact is avoided. This simplifies the approach considerably since we then do not need to deal with solid friction. Note that the model also allows to switch on the phase transformation kinetics (encoded in the dynamics of the phase-field function). In this case, the two bodies merge and move as a single solid body, again without the need for solid-solid friction.

If a point and its adjacent points are considered to be fluid, the lattice method is applied (see section 3.2.1). Near a solid surface, the bounce-back adds to the right-hand side of equation (18b) and accounts for fluid which ‘bounces back’ from the solid surface

$$f_i(\vec{x}, t + \Delta t) = \begin{cases} f_{-i}^*(\vec{x}, t) + g(\vec{x}, \vec{c}_i, \vec{u}_B, t) & \text{if } \vec{x} - \vec{c}_i \Delta t \text{ is solid} \\ f_i^*(\vec{x} - \vec{c}_i \Delta t, t) & \text{else} \end{cases}. \quad (23)$$

If no point $\vec{x} - \vec{c}_i \Delta t$ in the vicinity of \vec{x} is solid, the bounce-back is not calculated so that equations (18b) and (23) deliver the same result. However, if the point $\vec{x} - \vec{c}_i \Delta t$ lies within a solid body, there is no fluid population that can be streamed to point \vec{x} . Hence, the pseudo particles coming from the point $f_i(\vec{x})$ with the velocity \vec{c}_i are assumed to ‘bounce-back’ from the solid surface in the middle between the two points. Consequently, $f_{-i}^*(\vec{x}, t)$ denotes the population of the pseudo particles with the velocity $-\vec{c}_i$. If a solid surface is present in the vicinity, the corresponding part of the distribution function is reflected. The solid surface is here assumed to be in the middle between the fluid and the rigid body node at $\vec{x} - \vec{c}_i \Delta t / 2$. This adds to the consequence the remaining fluid has to be distributed to the neighboring points if a certain point changes from liquid to solid.

Further, we consider the movement of the solid body with the velocity \vec{u}_B . The movement of the solid body leads to a change of momentum of the adjacent fluid which is accounted for by

$$g(\vec{x}, \vec{c}_i, \vec{u}_B(\vec{x})) = \frac{2\rho(\vec{x})}{c_s^2} w_i \vec{c}_i \cdot \vec{u}_B(\vec{x} - \vec{c}_i \Delta t / 2) + \delta\rho(\vec{x}) \delta_{i0} \quad (24)$$

in equation (23). Whereas $\delta\rho(\vec{x})$ is an auxiliary term that ensures the local mass conservation with

$$\delta\rho(\vec{x}) = \frac{2\rho(\vec{x})}{c_s^2} w_i \vec{c}_i \cdot \vec{u}_B(\vec{x} - \vec{c}_i \Delta t / 2), \quad (25)$$

where the sum over i is executed for each point $\vec{x} - \vec{c}_i \Delta t$ that is solid so that the total change of mass caused by the first term in equation (24) is compensated. This mass correction $\delta\rho(\vec{x})$ is then added to the resting fluid population with the term δ_{i0} which is only non-zero for $i = 0$ so that no slip of the fluid along the solid surface is introduced.

The collision and bounce back of the fluid at the solid surface results in a momentum exchange between solid and fluid. The resulting local change of the momentum density $\Delta\vec{m}_B$ of the rigid body at a solid point \vec{x} is given by

$$\Delta\vec{m}_B(\vec{x}) = -\vec{c}_i [2f_i^*(\vec{x} + \vec{c}_i \Delta t) + g(\vec{x} + \vec{c}_i \Delta t, \vec{c}_i, \vec{u}_B)] \quad (26)$$

where the sum is executed for each point $\vec{x} + \vec{c}_i \Delta t$ that is fluid. By integration over the entire solid body B , corresponding total force \vec{F}_B and torque \vec{T}_B can then be obtained with

$$\vec{F}_B = \frac{1}{\Delta t} \int_B \Delta \vec{m}_B(\vec{x}) dV \quad (27a)$$

$$\vec{T}_B = \frac{1}{\Delta t} \int_B \left(\vec{x} - \vec{c}_i \frac{\Delta t}{2} - \vec{X}_B \right) \times \Delta \vec{m}_B(\vec{x}) dV, \quad (27b)$$

where \vec{X}_B denotes the center of mass of the solid body (see section 3.1.1).

Applying the bounce-back rule serves to ensure that fluid velocity is identical to that of the solid. However, as the solid body moves in space, a fluid node which is covered by the solid particle becomes part of the solid domain, while a node which is uncovered by solid retrieval is added to the fluid domain. Using the capillary bridge test, we have examined a number of ways to deal with this issue (see [31, 32] for an ample discussion of this issue) and find that various schemes produce qualitatively similar results, albeit quantitative differences exist in non-equilibrium effects (stresses and pressure gradients). In view of the fact that phase transformation in alloys are sensitive to concentration and density variations, and is thus of primary importance for the present project, while momentum fluctuations are less critical, we have chosen a strictly mass conserving scheme: The mass of a covered node is distributed among its immediate neighbors and an uncovered node is regarded as empty space. The only process which is allowed to change the liquid mass is via phase transformation, accounted for in the phase-field dynamics, $\phi(t)$. Importantly, since solid particles in this study move by orders of magnitude more slowly than the propagation of sound across the system, voids are quickly filled by mass transport from the surrounding liquid nodes.

Thus, if a fluid node at the point \vec{x}_n is covered by a solid particle, the populations $f_i(\vec{x}_n)$ are distributed among the neighboring fluid points via

$$f_i^{\text{new}}(\vec{x}) = f_i(\vec{x}) + \frac{f_i^{\text{eq}}(\rho(\vec{x}_m), \vec{u}(\vec{x}_m))}{|N_F(\vec{x}_m)|}, \quad (28)$$

where $N_F(\vec{x}_n)$ is the set of fluid neighbor nodes in a sphere of the radius R_A around \vec{x}_n with $N_F(\vec{x}_n) = \{\vec{x} \mid \|\vec{x}_n - \vec{x}\| \leq R_A \text{ and } \vec{x} \neq \vec{x}_n\}$. In our simulations, $R_A = \Delta x$ proves to be a good choice, which respects the local character of the process with relatively low noise. As mentioned above, in the case that a solid node becomes fluid, its density is set to zero.

3.2.3. Non-ideal fluids. In the following, we briefly present the implemented method to simulate liquid and vapor phase separation and their interaction with solid surfaces. For more detailed information, the reader is referred to [13, 14, 28, 33]. The liquid and vapor phase separation is introduced by a force density \vec{f} acting on the fluid (see equations (18) and (21)) with

$$\vec{f}(\vec{x}) = -\mathcal{G}\psi(\vec{x}) \sum_i w_i \psi(\vec{x} + \vec{c}_i \Delta t) \vec{c}_i, \quad (29)$$

where \mathcal{G} is a coupling constant and ψ a so-called lattice version of the mean-field potential,

$$\psi(\vec{x}) = 1 - e^{-\frac{\rho(\vec{x})}{\rho_0}}, \quad (30)$$

where ρ_0 is a reference density. The force density equation (29) can be interpreted as the sum of force densities which act between the pseudo particles at \vec{x} and the surrounding pseudo

particles at $\vec{x} + \vec{c}_i \Delta t$. Within this model, a convenient way to account for wetting effects is to identify a solid node as an immobile ‘fluid’ with a fictitious density ϱ_B . By the integration over all force densities between a fluid point \vec{x} and an adjacent point $\vec{x} + \vec{c}_i \Delta t$ of the rigid body B , the resulting force \vec{F}_B and torque \vec{T}_B acting on it can then be obtained

$$\vec{F}_B = -\mathcal{G} \int_F d\vec{x} \psi(\vec{x}) w_i \psi(\vec{x} + \vec{c}_i \Delta t) \vec{c}_i \quad (31a)$$

$$\vec{T}_B = -\mathcal{G} \int_F d\vec{x} \psi(\vec{x}) (\vec{x} + \vec{c}_i - \vec{X}_B) \times w_i \psi(\varrho_B) \vec{c}_i \quad (31b)$$

where again the sum over i is executed for each point $\vec{x} + \vec{c}_i \Delta t$ that is solid.

With $\vec{f} = -\nabla \cdot \underline{\underline{p}}$ it is possible to identify the corresponding pressure tensor

$$p_{ij} = \left[c_s^2 \rho + \frac{1}{2} c_s^2 \mathcal{G} \psi^2 + \frac{1}{2} c_s^4 \mathcal{G} \psi \Delta \psi + \frac{\mathcal{G} c_s^4}{4} |\nabla \psi|^2 \right] \delta_{ij} - \frac{1}{2} c_s^4 \mathcal{G} \partial_i \psi \partial_j \psi. \quad (32)$$

For the bulk pressure or the equation of states, one thus has

$$p = c_s^2 \rho + \frac{1}{2} c_s^2 \mathcal{G} \psi^2. \quad (33)$$

The pressure tensor can be used to calculate the surface tension. According to [34], the interface tension σ is given by the difference of the normal component of the pressure tensor p_\perp and its tangential component p_\parallel across the interface with

$$\sigma = \int_0^\eta dn (p_\perp - p_\parallel), \quad (34)$$

where n is the direction normal to the interface. If one considers only a planar interface, so that ψ changes only along the normal direction of the interface, the interface tension can be calculated with

$$\sigma = -\frac{1}{2} c_s^4 \mathcal{G} \int \left| \frac{\partial \psi}{\partial n} \right|^2 dn, \quad (35)$$

which is obtained by inserting equation (32) into equation (34).

Considering equations (35) and (30), one can see that the interface tension depends on the respective density profile. The density profile across the liquid–vapor interface is determined by the coupling constant \mathcal{G} . The density profile across the solid–vapor and the solid–liquid can be adjusted tuning the above introduced ‘solid density’ ϱ_B . This way, the contact angle of the solid body can be adjusted, and since the term ‘solid density’ is misleading in this context, we refer to ϱ_B as the wetting parameter. For a more detailed explanation, we refer the reader to [33].

3.3. Simulation procedure

As mention in section 3.1.1, we use a high-resolution scheme for the advection, equation (14), of the phase-fields with directional splitting and a monotonized central flux limiter [27]. This higher-order scheme serves to reduce the well-known numerical problem of diffuse interface spreading under advection. An advantage of the multi-phase-field method proposed here is that accounting for phase-field kinetics stabilizes the interface profile further, thus improving

numerical stability. As known from the standard literature on multi-phase-field [25, 26], the kinetics of ϕ read,

$$\dot{\phi}_\alpha = \sum_{\beta \neq \alpha}^N \frac{M_{\alpha\beta}}{N} \left(\left[\sigma_{\alpha\beta} (I_\alpha - I_\beta) + \sum_{\gamma \neq \alpha, \beta} (\sigma_{\beta\gamma} - \sigma_{\alpha\gamma}) I_\gamma \right] + \frac{\pi^2}{4\eta} \Delta g_{\alpha\beta} \right) \quad (36a)$$

$$I_\alpha = \nabla^2 \phi_\alpha + \frac{\pi^2}{\eta^2} \phi_\alpha, \quad (36b)$$

where $M_{\alpha\beta}$ is the mobility of the interface between phases α and β , $\sigma_{\alpha\beta}$ is the interface energy between the phase-fields and η is the interface width (see [26] for more details).

The restoration of the phase-field profile comes with a trade-off. Equation (36a) restores the phase-field profile but also introduces a shrinkage of the phase-field

$$\Delta \phi_\alpha = \int [\phi_\alpha(t_{\text{ref}}) - \phi_\alpha(t)] dV \quad (37)$$

according to the local curvature. Because of this shrinkage, the last term $\Delta g_{\alpha\beta}$ is necessary which is dynamically determined to conserve the volume of a phase-field ϕ_α with

$$\Delta g_{\alpha\beta} = -\Delta g_{\beta\alpha} = \frac{4\eta}{\pi^2} \frac{\Delta \phi_\alpha}{|\delta \phi_\alpha|}. \quad (38)$$

Similar as in section 3.1.2, $|\delta \phi_\alpha|$ denotes the number of nodes in the interface region of ϕ_α with $\delta \phi_\alpha = \{\vec{x} | 0.0 < \phi(\vec{x}) < 1.0\}$. To minimize this solid-phase sintering, we chose the phase-field mobility as small as reasonable.

If not stated otherwise, the following values of the introduced parameters have been used for the present simulations:

ρ_0	Reference density	1.000
ρ_L	Liquid density	1.888
τ	Relaxation time	1.100
\mathcal{G}	Coupling constant	-5.000
ρ_α	Mass density of ϕ_α	various
ϱ_α	Wetting parameter of ϕ_α	2.000
$M_{\alpha\beta}$	Phase-field mobility	10^{-5}
η	Phase-field interface width	5.000

4. Results

We first investigate the accuracy of the surface tension calculation in section 4.1. This investigation is the basis for the testing of the present model. In section 4.2, we test our model by the simulation of capillary bridges between two finite parallel plates. The results obtained from these simulations are compared with analytic solutions given in section 2.1.1. To demonstrate the capability to model the process of liquid-phase-sintering, we also investigate a more complicated situation in section 4.3, the dynamics of multiple particles connected by a capillary bridge. This investigation provides a first step towards the modeling of larger and more complex systems with more solid particles.

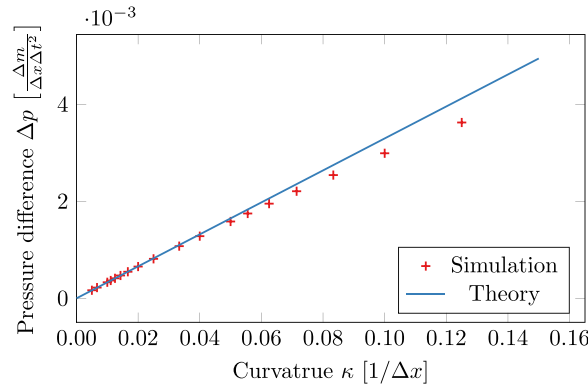


Figure 3. The figure shows the pressure difference between the vapor and the inside of a cylindrical liquid droplet for different radii which have been calculated from the simulation result with equation (33). The solid line shows the expected Laplace pressure equation (3) for a surface tension of $3.297 \cdot 10^{-2}$. This value of the surface tension has been calculated with equation (35).

4.1. Surface tension

In the following, we test the consistency of the surface tension calculations equation (35) with the Laplace pressure equation (3). By evaluating equation (35) for droplets of different radii, we obtained the value $3.297 \cdot 10^{-2}$ in lattice units for the surface tension. The value is used to predict the pressure gradient, by inserting it into equation (3). We show this prediction in figure 3. Also, the differences for different radii, obtained with equation (33), are depicted. One can see that the obtained pressure gradients are in agreement with the ones predicted by the Laplace pressure, equation (3). A deviation from the predicted value can be seen for large curvatures, which is expected because of the finite diffuse interface and the decreasing size of the droplets.

Another possibility to obtain the surface tension is to calculate the pressure gradient with equation (33) and use it together with the radius as input for equation (3) to calculate the resulting surface tension. This way, we yield $3.583 \cdot 10^{-2}$ for the value of surface tension which differs from the value obtained with equation (35) by approximately 8%. In the following chapter, we show that this value for the surface tension provides a better estimate for the acting capillary force on a solid body. Hence, $\sigma = 3.583 \cdot 10^{-2}$ is used in the following.

4.2. Capillary bridge between two plates

We continue the testing of the present model by investigating a capillary bridge between two finite parallel plates as schematically depicted in figure 1. The choice of finite plates ensures that the ambient pressure on both sides of the plate is the same. We use the analytic solution to approximate the resulting motion of the plates and compare them with the simulation results.

In section 2.1.2, we introduced the approximative solution equation (8) for the motion of the plates connected by a cylindrical capillary bridge and the analytic solution equation (7b) for the simple planar case. These solutions are a good approximation if the solid motion is slow and the fluid is near its equilibrium state. To realize this assumption in the simulation,

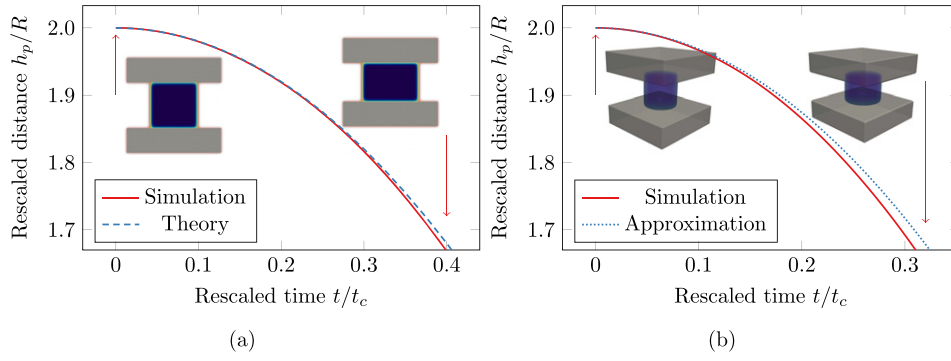


Figure 4. The temporal evolution of the distance between two plates connected by (a) a planar capillary bridge and (b) a cylindrical capillary bridge with a 90° wetting angle are shown. The distance h of the plates has been rescaled by the length R which is the initial radius of the cylindrical capillary bridge. Furthermore, we have rescaled the time by a characteristic time t_c with $t_c = \sqrt{m/\sigma}$ where m is the mass of the solid plates. For comparison, we show the theoretical expectations, equation (39a) in (a) and the approximation equation (39b). The simulation setups at $t = 0$ and the end of the displayed time interval are shown as insets. In both cases, the spatial discretization is the same with $\Delta x/R = 0.05$.

we assign to the solid a high mass density ρ_S as compared to the liquid mass density ρ_L with $\rho_S/\rho_L = 1.72 \cdot 10^4$. The initial simulation setup is schematically depicted for the planar setup in figure 1(a) and for the cylindrical setup in figure 1(b). Figure 4 shows the decreasing distance of the plates over time due to the action of the capillary force. The distance of the plates has been rescaled by the length R which is the initial radius of the cylindrical capillary bridge. Furthermore, we have rescaled the time by a characteristic time t_c with $t_c = \sqrt{m/\sigma}$ where m is the mass of the solid plates. By using R and t , one can rewrite equations (7b) and (8)

$$\frac{h_p}{R} = \frac{h_0}{R} - 2 \left(\frac{t}{t_c} \right)^2 \quad (39a)$$

$$\frac{h_c}{R} \approx \frac{h_0}{R} - \pi \left(\frac{t}{t_c} \right)^2. \quad (39b)$$

To obtain the rescaled equations of motion equation (39), we have assumed for the length of the planar capillary bridge that $L = R$. The simulation results are depicted in figure 4 together with the rescaled equations of motion equation (39). We also show as insets in figure 4 the particular simulation setups at $t = 0$ and at the end of the displayed time interval. A deviation of the simulations from the predictions is expected because the fluid motion has been neglected in the derivation of equation (39). Consequently, we show only the very beginning of the motion in figure 4 so that the theoretical prediction is accurate and can be used to test the simulations. One can see that in both cases, the planar one in figure 4(a) and the cylindrical one figure 4(b), the results agree with the predictions of equations (39a) and (39b) in the beginning. Nevertheless, for later times the simulation results deviate from the predictions. This effect is more significant in the cylindrical case than in the planar one.

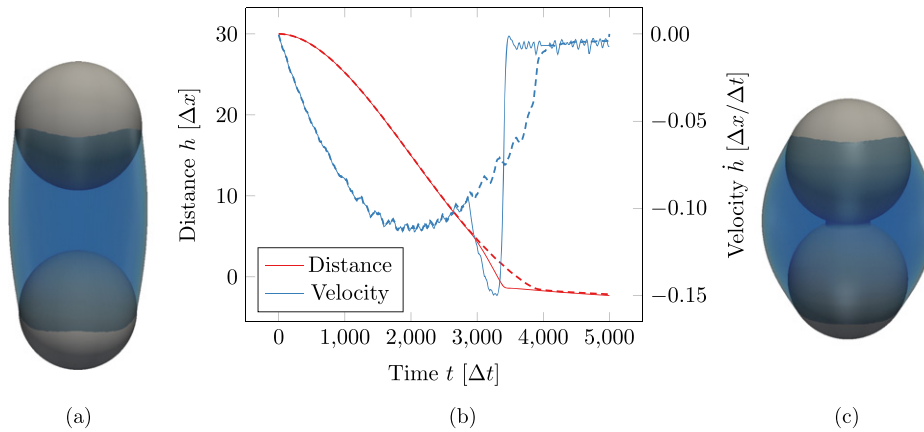


Figure 5. (a) Shows the simulation setup at $t = 0$ of the two solid particles with the radius $R = 30$ and the liquid–vapor interface, represented by the blue transparent isosurface. The amount of liquid has been chosen in such a way that the liquid volume fraction is exact $c = 0.5$ at $t = 0$. (b) Shows the closest distance h between the surfaces of the two spherical particles and the corresponding velocity \dot{h} . Also, the same simulation is shown as a dashed line but without the phase-field dynamics so that the solids do not undergo sintering. The steep change in velocity (solid blue line) is thus the result of sintering processes, which sets on as soon as the surfaces of particles come into contact. (c) Shows the simulation setup at $t = 5000$.

4.3. Dynamics of multiple particles

4.3.1. Two particles connected by a capillary bridge. We continue our investigation with two spherical particles connected by a capillary bridge with a particle radius of $R = 30$, mass density of $\rho = 4$, and liquid fraction of $c = 0.5$ (see figure 5). The closest distance between the particles h and the velocity \dot{h} are shown in figure 5. Because we want to consider solids with a very high wettability, a wetting-parameter of $\varrho_B = 2.0$ has been chosen. Above in Section 3.3, we have introduced the phase-field dynamics equation (36a) which models the physical process of sintering. To show the influence of the phase-field dynamics, the simulation has been performed twice, once with the phase-field dynamics and once without it where the phase-fields are only advected.

In figure 5, the closest distance between the surfaces of the particles h and the corresponding velocity \dot{h} are shown. The dashed lines in figure 5 indicate the simulations where the phase-fields are only advected. Without the phase-field dynamics, it takes more time for the two particles to come into contact with each other. The reason for this can be seen when looking at the velocity profile without the phase-field dynamics. In the beginning, the two particles are strongly accelerated towards each other, until about two thousand time steps when the velocity reaches its peak value (velocity minimum of the dashed line in figure 5). After two-thousand time-steps, the two particles are continuously decelerated until the particles come into contact. By looking at figure 2, one can see that there exists an equilibrium solution for $c = 0.5$ and low wetting angles where the particles are in contact. The existence of this equilibrium solution means that the capillary force must be attractive during the whole simulation time. Furthermore, the phase-fields are purely advected, and the solid–solid interaction has only a range of 3. Hence, the observed deceleration in figure 5 can only be caused

by the dynamics of the fluid. We do not consider an explicit drag force here. Consequently, the bounce-back effect equation (23) can only cause this deceleration.

When the phase-fields are not only advected (solid lines in figure 5), one can see that the time, until the two particles come into contact, is reduced. Even more visible is the influence of the phase-field dynamics in the velocity profile. At about $t = 3000$, the magnitude of the velocity increases strongly, and a short time after that the velocity drops to nearly zero. This strong acceleration occurs at about a distance of 10 and can be understood in the context of the phase-field method. The value of the present phase-fields varies continuously from 0 to 1 within a distance $\eta = 5$. This defines the interface thickness. Hence, the phase-fields begin to touch each other about a distance of $2\eta = 10$. At this distance, the phase-fields start to merge and form a common interface between the two solid particles.

When η is comparable to the width of a grain-boundary, the length-scale can be seen as physically meaningful, and the described process of merging can be regarded as the first step in the solid-phase sintering process. In contrast, if η is larger than a physical grain boundary width, the dynamics of the phase-field and the resulting variation of the distance below 2η shall be viewed as a numerical feature to model solid-phase sintering of larger scales.

At a distance below 2η , the phase-fields representing the particles start to deform. This occurs due to the solid-solid sintering process, where the particles reduce the surface area at the expense of a larger grain-boundary area. (The grain-boundary energy is assumed to be smaller than the surface energy). During this process, the centers of mass come closer together, as compared to hard and inert bodies at contact. This feature shows itself as a small negative distance in figure 5.

For more details about the modeling of surface diffusion with phase-field and the evolution of stress in two spherical particles undergoing the process of solid-phase sintering, the reader is referred to [20, 24, 35].

4.3.2. Effect of liquid fraction. Above, we investigated the dynamics of a capillary bridge between two spherical particles. A more intriguing investigation, however, is the influence of the liquid fraction on the dynamics of the system. The influence of the liquid fraction on the topology of a liquid bridge between two spheres has been shown above in section 2.2.

We start with two spherical particles with a radius of $R = 30$ and a mass density of $\rho = 4$ which are initialized with different amounts of liquid between them. We continue with the investigation of three and four particles, as a forecast of a system with many particles. Similar to Section 4.3.1, before the particles are allowed to move, the simulations run for fifteen thousand simulation time steps so that the liquid reaches its equilibrium shape. The time $t = 0$ refers to the point in time when the particles are allowed to move. Furthermore, we investigate here three different liquid fractions $c = 0.2$, $c = 0.3$, and $c = 0.5$. The simulation setup for $c = 0.2$ at $t = 0$ and $t = 5000$ are depicted as insets in the corresponding plots in figure 6. For a liquid fraction of $c = 0.5$, we show again a dashed line for a simulation where the phase-field dynamics, equation (36a), is switched off so that the phase-fields are purely advected.

We start the discussion with the concentration dependency of the distance and velocity profiles of two particles. In the case of a small amount of liquid ($c = 0.2$), the velocity of the particles increases linearly with time until they come into contact. For a liquid fraction of $c = 0.3$, one can see an increase in the velocity of the particles at the beginning, compared to the case of $c = 0.2$. By looking at the velocity profile of $c = 0.5$, the particles are more strongly accelerated at the beginning than for $c = 0.2$, but for later times one can see a clear deceleration. To show this more clearly, we also plot the velocity profile corresponding to the case where the phase-fields are purely advected (dashed-line). By comparing the dashed and

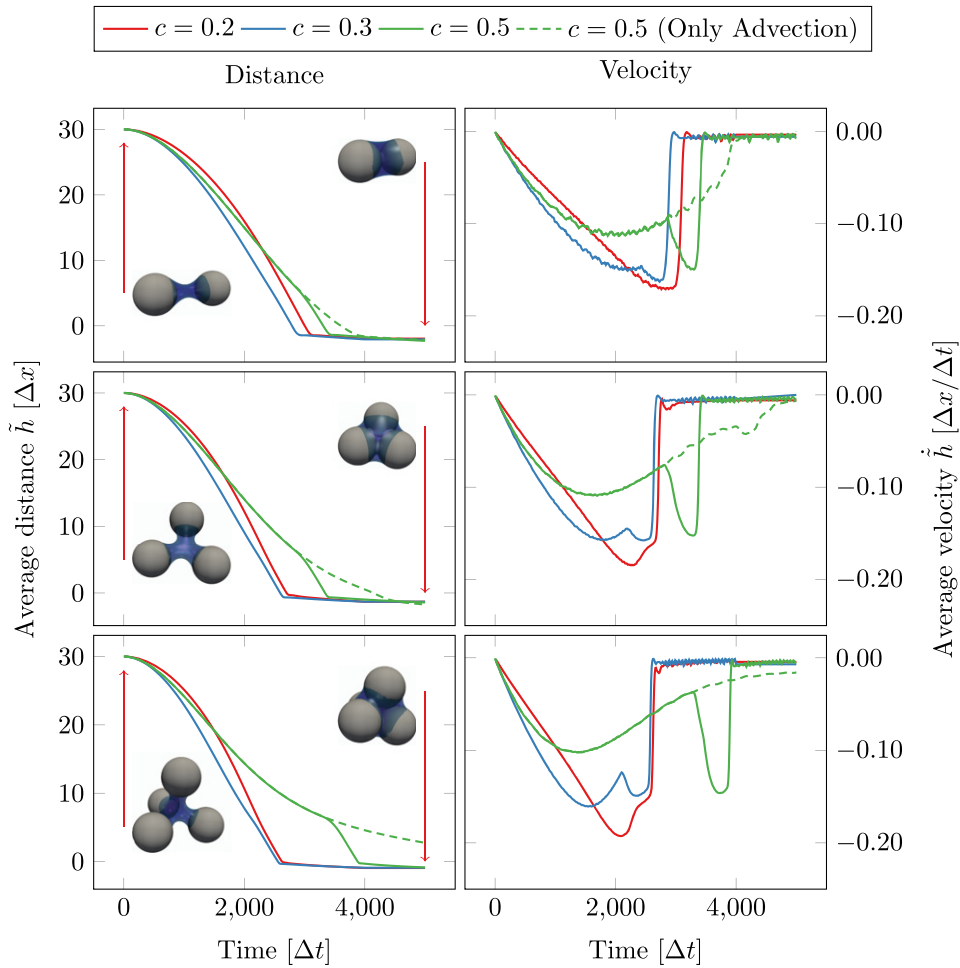


Figure 6. In the first row, the distance (left) and the velocity (right) of two spherical particles are shown which have the radius $R = 30$ and are connected by a capillary bridge. The amounts of liquid are chosen in such a way that at $t = 0$ three different liquid to solid volume fractions are investigated, $c = 0.2$, $c = 0.3$, and $c = 0.5$. As inset picture, we show the configurations of the liquid and the solid particles at $t = 0$ and $t = 5000$ for a liquid fraction $c = 0.2$. Likewise, the second row shows the average distance and velocity of three particles forming an equilateral triangle. In the third row the results of four-particles forming a tetrahedron are shown.

the solid lines of the velocity profile, one can see that the strong acceleration followed by an even stronger deceleration is caused by the dynamics of the phase-field. This process of deceleration for larger amounts of liquids, $c = 0.2$ and $c = 0.3$, can be explained as the effect of drag (see section 4.3.1). In figure 6, one can see that the effect of drag is more significant for larger amounts of liquid, as to be expected.

By looking at the distance or velocity profiles in figure 6, one can easily identify the time when the particles are in contact. In the velocity profile, this point in time is indicated by the steep drop of the velocity to zero. The contact time is the shortest for a liquid fraction of

$c = 0.3$ and the largest for $c = 0.5$. This observation is also true for the three and four-particle systems.

In the second setup, we placed three spherical particles, with the same radius and distance as in the first case, in such a way that they form an equilateral triangle. Different amounts of liquid are initialized in the center of the triangle so that the resulting liquid volume fractions are the same as in the first case. Figure 6 shows the decreasing average distance $\bar{h} = 1/3 \sum_i h_i$ between the three particles. Because the particles form an equilateral triangle, the force on each particle is the same, and hence the particles form an equilateral triangle during the entire simulation. This means that the average distance is equal to the distance between the particle $\bar{h} = h_2 = h_3 = h_3$.

The results we obtain for three particles are qualitatively similar to the results obtained for two particles. However, one can see that the time, until the particles come into contact, is reduced for $c = 0.2$ and $c = 0.3$. In the case of $c = 0.5$, the effect of drag is stronger than in the case of two particles.

In the last setup, we placed four spherical particles, with the same radius and distance as in the first case, in such a way that they form a tetrahedron. Again, we have initialized spherical liquid drops of different sizes in the center of the tetrahedron and waited for ten thousand simulation time steps so that the liquid reaches its equilibrium before the particles are allowed to move ($t = 0$). Likewise, figure 6 shows the decreasing average distance $\bar{h} = 1/4 \sum_i h_i$ between the particles for different liquid volume fractions.

The results we obtain for four particles are qualitatively similar to the results obtained for two and three particles. The time until the particles come into contact is reduced for $c = 0.2$ and $c = 0.3$ compared to two particles but is comparable to the case of three particles. Furthermore, the above-discussed effect of drag is even stronger than in the case of three particles. The fact that the effect of drag increases with the number of particles can be explained by the higher amount of solid surface in contact with the liquid which leads to a higher drag force.

5. Summary and outlook

We present a combined phase-field-lattice Boltzmann model for the simulation of liquid state sintering. The accuracy of the present method is carefully investigated by considering a liquid bridge between two parallel plates of finite size. We show that the obtained results for their motion are in agreement with the present theoretical predictions. The capability of the present model to simulate liquid state sintering is demonstrated by the investigation of the dynamics of two, three, and four solid particles under the action of a capillary attraction between them. In all the cases investigated, increasing the amount of liquid first accelerates the compaction process.

A liquid fraction higher than a certain threshold, however, slows down the motion of spheres and leads to an increase of the time necessary for the particles to come into contact. We show that this is caused by the dynamics of the fluid, i.e. viscous drag. There is thus an optimum choice for liquid content concerning the compaction process. The exact value of this optimum parameter will depend in general on the powder packing fraction, grain shape, and size distribution.

Throughout the entire process of liquid phase sintering, thermal effects are of great importance as they play a key role for many issues such as diffusion (which influences, e.g., the initial solid-phase sintering stage), thermodynamic driving forces (e.g., chemical potentials) for sintering and dissolution strength of hard metal component in the soft-metal liquid. Adding a diffusion solver to the present modular code will promote the present method to an efficient tool to study these interesting effects.

On the methodological side, there is also room for new developments. A possible direction here would be to address both multi-phase flows as well as phase transformation kinetics within a multi-phase-field framework. As a first step along this line, we have proposed a phase-field-based liquid-vapor model for binary phases to study metallic foams [36]. A natural next step would be an extension to the multi-phase-field level including solidification and solid–fluid interactions.

Acknowledgments

Financial support by the German Research Foundation DFG under the Grant VA205/17–1 is gratefully acknowledged.

Appendix A. Liquid bridge between two plates—force

We consider a cylindrical capillary between two finite plates. As shown above, the change of internal energy is given by $dU = \sigma dA$ with $A = 2\pi R$ one obtains $dU = 2\pi\sigma dR$. Further, we consider the energy of the liquid phase U_L as a function of the distance h_c between the two plates. Because the liquid volume is constant $V_L = \pi R_0^2 h_0 = \pi R^2 h_c$, the radius R can be expressed as function of the initial radius R_0 , initial distance h_0 and distance h_c with $R = R_0 \sqrt{h_0/h_c}$. Hence, the force is obtained as

$$F = \left(\frac{dU}{dh_c} \right)_{V_L} = \pi\sigma R_0 \sqrt{h_0/h_c}. \quad (\text{A.1})$$

Appendix B. Liquid bridge between two solid spheres

B.1. Spherical bridge

Equation (9) describes the necessary wetting angle to form a spherical capillary bridge as a function of the liquid fraction. To derive this relation, we consider two spherical solid bodies in contact, as depicted in figure B1.

B.1.1. Small spherical capillary bridge. The contact angle Θ_S is defined as the angle between the tangent lines of the liquid and solid surface at the triple point. It is thereby equal to the angle between the surface normals vectors of the liquid and solid surface at the triple point and can be calculated with

$$\Theta_S = \theta_2 - \theta_1, \quad (\text{B.1})$$

where θ_1 and θ_2 are the angles between the surface normals and the depicted dashed line (see figure B1). These angles can be calculated by

$$\theta_1 = \arccos \left(\frac{R_S - h_S}{R_S} \right) \quad (\text{B.2a})$$

$$\theta_2 = \pi - \arccos \left(\frac{h_S}{\chi_S R_S} \right), \quad (\text{B.2b})$$

where $\chi_S \in [0, 2]$ is a dimensionless scaling factor. We introduced this scaling factor in order to relate the radius of the capillary bridge R_L to the radius of the solid spheres R_S with $R_L = \chi_S R_S$.

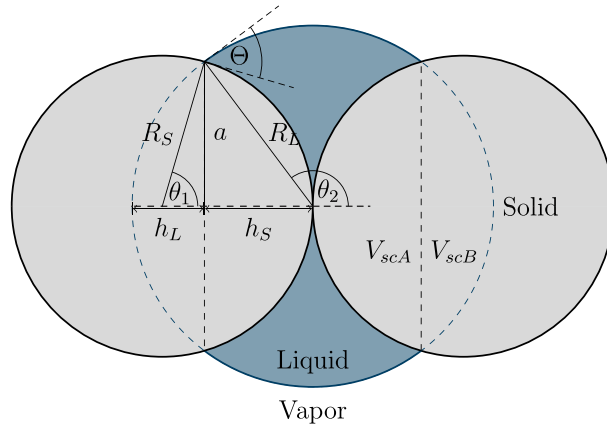


Figure B1. Depicted are two spherical solid bodies with equal radii R_S . The two bodies are in contact with each other and are connected by a liquid spherical capillary bridge with the radius $R_L = \chi_S R_S$. The figure has been generated with the parameter $\chi_S = 1.2$.

Again, one can obtain a system of equations for the side lengths of the depicted triangles by using the Pythagorean theorem,

$$\chi_S R_S = h_L + h_S \quad (\text{B.3a})$$

$$R_S^2 = a^2 + (R_S - h_S)^2 \quad (\text{B.3b})$$

$$\chi_S^2 R_S^2 = a^2 + h_S^2, \quad (\text{B.3c})$$

with the solution

$$h_S = \frac{\chi_S^2}{2} R_S \quad (\text{B.4a})$$

$$h_L = \frac{2\chi_S - \chi_S^2}{2} R_S \quad (\text{B.4b})$$

$$a = \frac{1}{2} \sqrt{4\chi_S^2 - \chi_S^4} R_S. \quad (\text{B.4c})$$

In equation (B.4), we expressed the geometric parameters depicted in figure B1 as function of the radius R_S and the scaling parameter χ_S . As to be expected, the contact angle can be expressed as a function of χ_S with

$$\Theta_S = \arccos\left(\frac{\chi_S^2}{2} - 1\right) - \arccos\left(\frac{\chi_S}{2}\right). \quad (\text{B.5})$$

Furthermore, we replace the scaling factor χ_S by the liquid volume fraction c . Therefore, the volume of the liquid has to be calculated by subtracting the volume of the spherical caps V_{scA} and V_{scB} (see figure B1) from the volume of a liquid sphere V_{L_S} with

$$V_L = V_{L_S} - 2V_{scA} - 2V_{scB} \quad (\text{B.6})$$

and

$$V_{L_S} = \frac{4\pi}{3} \chi_S^3 R^3 \quad (\text{B.7a})$$

$$V_{scA} = \frac{\pi}{3} h_S^2 (3R_S - h_S) \quad (\text{B.7b})$$

$$V_{scB} = \frac{\pi}{3} h_L^2 (3\chi_S R_S - h_L) \quad (\text{B.7c})$$

and equation (B.4).

The volumes of the spherical caps, V_{scA} and V_{scB} , can be parametrized with R_S and χ_S by inserting equation (B.4a) into equation (B.7b) and equation (B.4b) into equation (B.7c) so that

$$V_{scA} = \pi R_S^3 \left(-\frac{1}{24} \chi_S^6 + \frac{1}{4} \chi_S^4 \right) \quad (\text{B.8a})$$

$$V_{scB} = \pi R_S^3 \left(\frac{1}{24} \chi_S^6 - \frac{1}{2} \chi_S^4 + \frac{2}{3} \chi_S^3 \right). \quad (\text{B.8b})$$

Inserting equations (B.8a), (B.8b), and (B.7a) into equation (B.6) delivers a simple parametrization for the liquid volume

$$V_L = \frac{1}{2} \pi \chi_S^4 R_S^3. \quad (\text{B.9})$$

The same way as for the cylindrical bridge, we can calculate the liquid volume fraction with

$$c = \frac{V_L}{V_L + V_S} \quad (\text{B.10a})$$

$$= \frac{3\chi_S^4}{3\chi_S^4 + 16}. \quad (\text{B.10b})$$

By rearranging the terms of equation (B.10), we obtain a fourth order polynomial equation for χ_S

$$\chi_S^4 = \frac{16c}{3(1-c)}, \quad (\text{B.11})$$

which has a real and positive solution

$$\chi_S = \frac{2}{\sqrt[4]{3}} \frac{\sqrt{(1-c)} \sqrt{c(1-c)}}{1-c}. \quad (\text{B.12})$$

Inserting equation (B.12) into equation (B.5) delivers the solution shown in figure 2.

B.1.2. Large spherical capillary bridge. In the case of relatively large amount of liquid, a liquid bridge as depicted in figure B2 may form. The angles θ_1 and θ_2 are obtained in the same manner as above with

$$\Theta_S = \theta_2 - \theta_1 \quad (\text{B.13a})$$

$$\theta_1 = \pi - \arccos \left(\frac{h_S - R_S}{\chi_S R_S} \right) \quad (\text{B.13b})$$

$$\theta_2 = \pi - \arccos \left(\frac{h_S}{R_S} \right), \quad (\text{B.13c})$$

where θ_1 can be simplified to

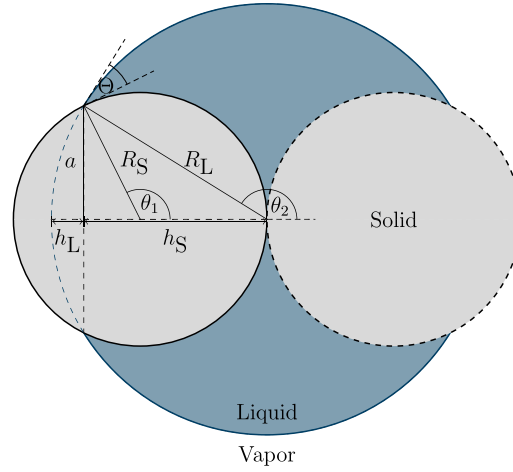


Figure B2. Depicted are two spherical solid bodies with equal radii R_S . The bodies are in contact with each other and are connected by a liquid spherical capillary bridge with the radius $\chi_S R_S$ and the contact angle Θ . The figure has been generated with the parameter $\chi_S = 1.7$.

$$\theta_1 = \arccos\left(\frac{R_S - h_S}{\chi_S R_S}\right). \quad (\text{B.14})$$

The height h_S can be calculated in the same manner as in appendix B.1.1, and equation (B.5) can be obtained again.

B.2. Cylindrical bridge

Equation (10) describes the wetting angle necessary to form a cylindrical capillary bridge as a function of the liquid fraction. To derive this relation, we consider two spherical solid bodies in contact, as depicted in figure B3. To calculate the contact angle Θ_c , we consider the angle θ between two lines. The first line starts at the center of the sphere A ends in the triple point B . The second line also starts at the center of the sphere A but ends in the contact point C between the spheres so that $\theta = \arccos\left(\frac{R-h}{R}\right)$, where h is half of the height of the cylindrical capillary bridge. By considering the intercept theorem, we obtain the contact angle

$$\Theta_c = \frac{\pi}{2} - \arccos(1 - \chi_c), \quad (\text{B.15})$$

where we have introduced the dimensionless scaling parameter $\chi_c \in [0, 1]$ with $h = \chi_c R$.

The volume of the liquid can be determined by calculating the volume of a cylinder and subtraction of the solid sphere caps, which cover part of the cylinder's volume,

$$V_L = V_{\text{cylinder}} - 2V_{\text{sphere-cap}} \quad (\text{B.16a})$$

$$= 2\pi R_S^2 h - 2\frac{\pi}{6} h [3R_S^2 + h^2] \quad (\text{B.16b})$$

$$= \pi R_S^2 h - \frac{\pi}{3} h^3. \quad (\text{B.16c})$$

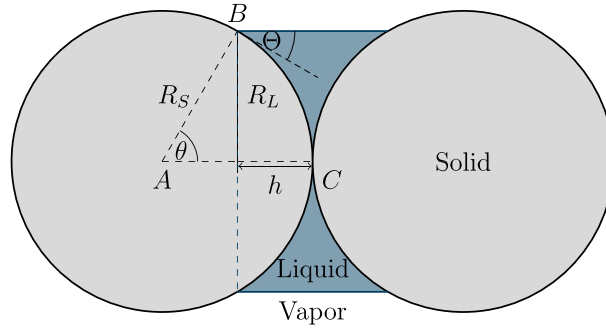


Figure B3. Depicted are two spherical solid bodies with the radius R_S . The two bodies are in contact with each other and are connected by a liquid cylindrical capillary bridge with the radius R_L , the height $2h$, and the contact angle Θ .

By using the Pythagorean theorem $R^2 = R_S^2 + (R - h)^2$, the radius of the capillary bridge R_S in equation (B.16c) can be replaced by the radius of the solid sphere R_S . With this replacement, we obtain for the fluid volume

$$V_L = 2\pi R h^2 - \frac{4}{3}\pi h^3. \quad (\text{B.17})$$

Furthermore, we replace height h again with $h = \chi_c R$ so that the expression for the fluid volume

$$V_L = \left(-\frac{4}{3}\chi_c^3 + 2\chi_c^2 \right) \pi R^3 \quad (\text{B.18})$$

can be further simplified. With equation (B.18) and the volume of the solid, $V_S = \frac{8}{3}\pi R^3$, the liquid volume fraction can be calculated

$$c = \frac{V_L}{V_L + V_S} \quad (\text{B.19a})$$

$$= \frac{2\chi_c^3 - 3\chi_c^2}{2\chi_c^3 - 3\chi_c^2 - 4}. \quad (\text{B.19b})$$

Equation (B.19b) can be transformed in a third order polynomial

$$\chi_c^3 - \frac{3}{2}\chi_c^2 + \frac{2c}{1-c} = 0. \quad (\text{B.20})$$

The polynomial equation (B.20) has three real roots for $c \in (0, 0.2)$. By substituting $\chi_c = t + \frac{1}{2}$, we can write equation (B.20) in the form,

$$t^3 + pt + q = 0 \quad (\text{B.21})$$

with $p = -\frac{1}{4}$ and $q = \frac{2c}{1-c} - \frac{1}{4}$. With the use of the cosine power rule

$$\cos^3(\eta) - \frac{3}{4}\cos(\eta) - \frac{1}{4}\cos(3\eta) = 0, \quad (\text{B.22})$$

we find three real solutions of equation (B.21)

$$t_n = \sqrt{-\frac{4p}{3}} \cos \left(\frac{1}{3} \arccos \left[-4q \left(-\frac{4p}{3} \right)^{\frac{3}{2}} \right] + \frac{2n\pi}{3} \right) \quad (\text{B.23})$$

with $n \in \{0, 1, 2\}$. By back substitution, we also obtain three real solutions for the scaling factor

$$\chi_{cn} = -\cos \left(\frac{1}{3} \arccos \left(\frac{1-9c}{1-c} \right) + \frac{2n\pi}{3} \right) + \frac{1}{2}. \quad (\text{B.24})$$

The physically meaningful solution of χ_c has to be limited to the interval $[0, 1]$, which is only fulfilled by χ_{c2} . Inserting equation (B.24) into equation (B.15) delivers the result shown in figure 2.

ORCID iDs

Raphael Schiedung  <https://orcid.org/0000-0002-5332-4987>

References

- [1] Heady R B and Cahn J W 1970 An analysis of the capillary forces in liquid-phase sintering of spherical particles *Metall. Trans.* **1** 185–9
- [2] Lian G, Thornton C and Adams M J 1993 A theoretical study of the liquid bridge forces between two rigid spherical bodies *J. Colloid Interface Sci.* **161** 138–47
- [3] Rabinovich Y I, Esayanur M S and Moudgil B M 2005 Capillary forces between two spheres with a fixed volume liquid bridge: theory and experiment *Langmuir* **21** 10992–7
- [4] Megias-Alguacil D and Gauckler L J 2009 Capillary forces between two solid spheres linked by a concave liquid bridge: regions of existence and forces mapping *AIChE J.* **55** 1103–9
- [5] Chen Y, Zhao Y, Gao H and Zheng J 2011 Liquid bridge force between two unequal-sized spheres or a sphere and a plane *Particuology* **9** 374–80
- [6] Payam A F and Fathipour M 2011 A capillary force model for interactions between two spheres *Particuology* **9** 381–6
- [7] Villanueva W, Grönhagen K, Amberg G and Ågren J 2009 Multicomponent and multiphase simulation of liquid-phase sintering *Comput. Mater. Sci.* **47** 512–20
- [8] Medvedev D, Varnik F and Steinbach I 2013 Simulating mobile dendrites in a flow *Procedia Computer Science* **18** 2512–20
- [9] Subhedar A, Steinbach I and Varnik F 2015 Modeling the flow in diffuse interface methods of solidification *Phys. Rev. E* **92** 023303
- [10] Stratford K, Adhikari R, Pagonabarraga I and Desplat J-C 2005 Lattice Boltzmann for binary fluids with suspended colloids *J. Stat. Phys.* **121** 163–78
- [11] Stratford K and Pagonabarraga I 2008 Parallel simulation of particle suspensions with the lattice Boltzmann method *Comput. Math. Appl.* **55** 1585–93
- [12] Connington K W, Lee T and Morris J F 2015 Interaction of fluid interfaces with immersed solid particles using the lattice Boltzmann method for liquid–gas–particle systems *J. Comput. Phys.* **283** 453–77
- [13] Shan X and Chen H 1993 Lattice Boltzmann model for simulating flows with multiple phases and components *Phys. Rev. E* **47** 1815
- [14] Shan X and Chen H 1994 Simulation of nonideal gases and liquid–gas phase transitions by the lattice Boltzmann equation *Phys. Rev. E* **49** 2941
- [15] Al-Ghoul M, Boon J P, Coveney P V, Harting J, Venturoli M and Coveney P V 2004 Large-scale grid-enabled lattice Boltzmann simulations of complex fluid flow in porous media and under shear *Phil. Trans. R. Soc. A* **362** 1703–22
- [16] Liu H, Kang Q, Leonardi C R, Schmieschek S, Narváez A, Jones B D, Williams J R, Valocchi A J and Harting J 2016 Multiphase lattice Boltzmann simulations for porous media applications *Comput. Geosci.* **20** 777–805

- [17] Günther F, Janoschek F, Frijters S and Harting J 2013 Lattice Boltzmann simulations of anisotropic particles at liquid interfaces *Comput. Fluids* **80** 184–9
- [18] Davies G B, Krüger T, Coveney P V, Jens Harting J and Fernando Bresme F 2014 Assembling ellipsoidal particles at fluid interfaces using switchable dipolar capillary interactions *Adv. Mater.* **26** 6715–9
- [19] Sun X and Sakai M 2016 Direct numerical simulation of gas-solid-liquid flows with capillary effects: an application to liquid bridge forces between spherical particles *Phys. Rev. E* **94** 063301
- [20] Schiedung R, Kamachali R D, Steinbach I and Varnik F 2017 Multi-phase-field model for surface and phase-boundary diffusion *Phys. Rev. E* **96** 012801
- [21] Kralchevsky P and Nagayama K 2001 *Particles at Fluid Interfaces and Membranes: Attachment of Colloid Particles and Proteins to Interfaces and Formation of Two-Dimensional Arrays* 1st edn (Amsterdam: Elsevier)
- [22] Steinbach I 2008 Effect of interface anisotropy on spacing selection in constrained dendrite growth *Acta Mater.* **56** 4965–71
- [23] Kamachali R D and Steinbach I 2012 3-D phase-field simulation of grain growth: topological analysis versus mean-field approximations *Acta Mater.* **60** 2719–28
- [24] Schiedung R, Steinbach I and Varnik F 2018 Multi-phase-field method for surface tension induced elasticity *Phys. Rev. B* **97** 035410
- [25] Steinbach I 2009 Phase-field models in materials science *Modelling Simul. Mater. Sci. Eng.* **17** 073001
- [26] Ingo Steinbach 2013 Phase-field model for microstructure evolution at the mesoscopic scale *Annu. Rev. Mater. Res.* **43** 89–107
- [27] Leer B V 1977 Towards the ultimate conservative difference scheme. IV. A new approach to numerical convection *J. Comput. Phys.* **23** 276–99
- [28] Montessori A, Falcucci G, La Rocca M, Ansumali S and Succi S 2015 Three-dimensional lattice pseudo-potentials for multiphase flow simulations at high density ratios *J. Stat. Phys.* **161** 1404–19
- [29] Guo Z, Zheng C and Shi B 2002 Discrete lattice effects on the forcing term in the lattice Boltzmann method *Phys. Rev. E* **65** 046308
- [30] Aidun C K and Lu Y 1995 Lattice Boltzmann simulation of solid particles suspended in fluid *J. Stat. Phys.* **81** 49–61
- [31] Ladd A J C and Verberg R 2001 Lattice-Boltzmann simulations of particle-fluid suspensions *J. Stat. Phys.* **104** 1191–251
- [32] Krüger T, Kusumaatmaja H, Kuzmin A, Shardt O, Silva G and Vignon E M 2017 *The Lattice Boltzmann Method* (Berlin: Springer)
- [33] Benzi R, Biferale L, Sbragaglia M, Succi S and Toschi F 2006 Mesoscopic modeling of a two-phase flow in the presence of boundaries: the contact angle *Phys. Rev. E* **74** 021509
- [34] Rowlinson J S and Widom B 1982 *Molecular Theory of Capillarity (The International Series of Monographs on Chemistry)* (Oxford: Clarendon)
- [35] Julia K, Hassan S, Schiedung R and Steinbach I 2018 Phase-field modeling of pores and precipitates in polycrystalline systems *Modelling Simul. Mater. Sci. Eng.* **26** 065003
- [36] Vakili S, Steinbach I and Varnik F 2020 Controlling bubble coalescence in metallic foams: a simple phase field-based approach *Comput. Mater. Sci.* **173** 109437